IEEE Photonics Journal
An IEEE Photonics Society Publication

Open Access

# Optimization of Hybrid Silicon Lasers for High-Speed Direct Modulation

Volume 7, Number 2, April 2015

**Yu Lian Cao**
**Xiao Nan Hu**
**Yuan Bing Cheng**
**Hong Wang**
**Qi Jie Wang**

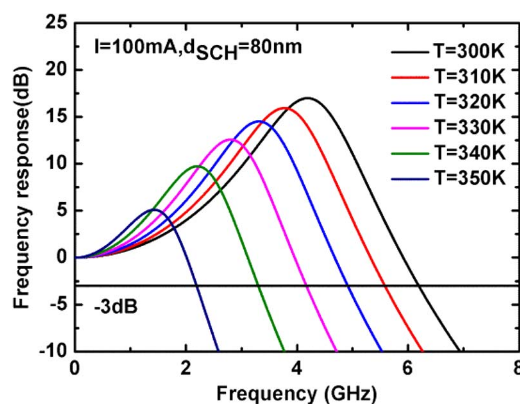


DOI: 10.1109/JPHOT.2015.2404531
1943-0655 © 2015 IEEE

IEEE photonics SOCIETY

IEEE

# Optimization of Hybrid Silicon Lasers for High-Speed Direct Modulation

**Yu Lian Cao,[1,2] Xiao Nan Hu,[1] Yuan Bing Cheng,[1] Hong Wang,[1] and Qi Jie Wang[1,3]**

[1]OPTIMUS, School of Electrical and Electronic Engineering, Nanyang Technological University, Singapore 639798
[2]Nano-Optoelectronics Laboratory, Institute of Semiconductors, Chinese Academy of Sciences, Beijing 100083, China
[3]Centre for Disruptive Photonic Technology, School of Physical and Mathematical Sciences, Nanyang Technological University, Singapore 6373718

*DOI: 10.1109/JPHOT.2015.2404531*
*1943-0655 © 2015 IEEE. Translations and content mining are permitted for academic research only. Personal use is also permitted, but republication/redistribution requires IEEE permission. See http://www.ieee.org/publications_standards/publications/rights/index.html for more information.*

Manuscript received January 18, 2015; revised February 11, 2015; accepted February 11, 2015. Date of publication February 16, 2015; date of current version March 11, 2015. This work is supported by grants funded by Ministry of Education, Singapore (MOE2011-T2-2-147), A*STAR SERC Future Data Center Technologies (Grant No. 112 280 4038), and A*STAR - MINDEF Science and Technology Joint Funding Programme (Grant No. 122 331 0076). Corresponding author: Q. J. Wang (e-mail: qjwang@ntu.edu.sg).

**Abstract:** We report the optimization of hybrid silicon lasers for high-speed direct modulations by studying the small- and large-signal modulation responses based on the simple carrier transport model in this paper. The theoretical model matches well with published experimental data as the same structure parameters are used. To investigate the strong heating effect in hybrid lasers, we apply all of the carrier diffusion/capture and thermionic escape lifetimes to be temperature dependent in simulations. The frequency response of the small-signal analysis shows that the modulation bandwidth is much more sensitive to the temperature and the separate confinement heterostructure (SCH) thickness compared with the other limiting factors, such as the confinement factor, the interlayer thickness, etc. The largest modulation bandwidth decreases from 6.2 to 2.2 GHz under an injection current of 100 mA and an SCH thickness of 80 nm when the temperature rises from 300 to 350 K. The modulation speed will be greatly improved with a thinner SCH layer, particularly the p-type SCH layer, which helps shorten the diffusion lifetime. Furthermore, eye diagrams are also calculated under different bit rates, SCH thicknesses, and temperatures, respectively. With the increase of the temperature or SCH thickness, the quality of eye diagrams becomes worse. It shows that the modulation frequency can reach 10 Gb/s. We believe that this paper can serve as a guideline for the optimization of next-generation high-speed modulated hybrid silicon lasers.

**Index Terms:** Hybrid silicon lasers, high-speed modulation, relaxation frequency, damping rate.

## 1. Introduction

The recent development of silicon photonic circuits has attracted great attention due to their advantages of broad bandwidth and large capacity compared with electronic circuit counterparts. Extremely compact photonic integrated circuits (PIC) in the silicon-on-insulator (SOI) platform can be made by the complementary metal oxide semiconductor (CMOS) compatible

processes [1]. A PIC should include various functions such as light generation, waveguiding, modulation, amplification, and detection. Passive devices, such as waveguides, array waveguide gratings, multi-mode interference (MMI) coupler, vertical couplers, and filters on SOI wafers have shown satisfactory performance [2]–[5]. However, although indispensable in an active PIC, direct generation of light in silicon is inherently a challenge due to the indirect bandgap of silicon. To overcome this limitation, heterogeneous integration of III–V semiconductors lasers on top of a SOI wafer, the so called hybrid laser [6], has been demonstrated. There are mainly two methods to integrate III–V semiconductor material on silicon (Si): the epitaxial growth of III–V laser on Si and the integration of III–V gain materials on silicon via die or wafer bonding techniques. The epitaxial growth of III–V laser on Si substrates is still a major challenge because of large mismatch in lattice constants and thermal expansion coefficients between the III–V and Si. Integration of III–V gain materials on silicon via die or wafer bonding technique is quite promising, as it allows a high density of integration, collective processing and the use of high-quality III–V layers. The laser structure can be designed to ensure a direct evanescent coupling of the light into the silicon waveguide underneath.

The first electrically pumped Fabry–Pérot (FP) cavity hybrid lasers on SOI was demonstrated based on molecular bonding by the UCSB and Intel groups in 2006 [6]. After that, various kinds of hybrid lasers, such as racetrack [7], Distributed Feedback Bragg (DFB) and Distributed Bragg Reflector (DBR) lasers have been reported [8]–[10]. In [10], the 3 dB bandwidth of around 7 GHz is achieved in hybrid lasers. However, there are still many challenges for applying hybrid lasers directly into optical communication systems. High-speed direct modulation is one of the main concerns. The main advantage of the direct modulation technique is its simplicity. However, high-speed frequency modulation in hybrid lasers is limited by two factors. Firstly, the device size of hybrid laser is large due to the limitation of the confinement factor in the III–V gain material, which reduces the relaxation oscillation frequency and increases the parasitic capacitance of the hybrid laser. This will affect the direct modulation speed of the hybrid lasers. Secondly, poor thermal conductivity of $SiO_2$ beneath Si causes severe heat accumulation, which has been verified by the thermal rollover occurred in the light power versus current curves [6]–[9]. Poor heat dissipation decreases the differential gain and the relaxation frequency of hybrid lasers, which in turn reduce the direct modulation speed of the hybrid lasers. Thus, in our calculations, to study the strong heating effect, we apply the parameters such as diffusion, capture times, and thermionic escape times to be temperature dependent for the full investigations of the unique characteristics of hybrid laser. This is different from the models in [11] and [12], where the carrier capture rate and escape rate are fixed as a constant. In hybrid lasers, these two temperature-dependent factors will affect the modulation responses greatly under high speed modulations.

In order to simulate the modulation bandwidth of the hybrid lasers, high speed direct modulation response of hybrid lasers operating at 1.55 $\mu$m is investigated based on the carrier transport model in this paper. Two kind of simulations, small and large modulations, are considered. To the best of our knowledge, this is the first investigation about quantitative calculation and discussions on the direct modulation characteristics of hybrid lasers [11]. Some design criteria for optimizing hybrid lasers on SOI for high speed operation are presented.

This paper is organized as follows. In Section 2, the modulation carrier transport model is developed based on the rate equation theory. In Section 3, the small signal modulation response of hybrid lasers is analyzed under different working temperatures, confinement factors, separate confinement heterostructure (SCH) layer thicknesses and injection currents. Finally, eye diagrams for large signal modulations are simulated. In Section 4, the results are summarized.

## 2. Rate Equations

A typical SCH single quantum well (QW) laser is shown in Fig. 1, where the thickness of the arrow indicates the amount of carriers in different regions. This also represents the structure that is used in the multiple quantum well lasers. In this work, we investigate the carrier transport

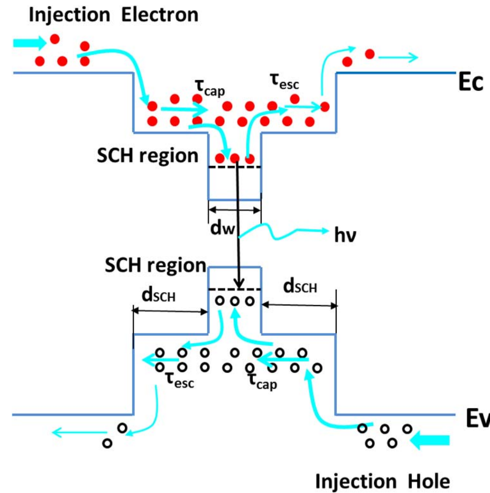


Fig. 1. Carrier transports in the carrier transport model, where the thickness of the arrow represents the amount of carriers in different regions.

(diffusion, capture, and escape) in such a laser structure and analyze its effects on the small signal modulation under electrical injection [12]–[15].

The rate equations are written as

$$\frac{dn_1}{dt} = \frac{I}{q_e V} - \frac{n_1}{\tau_{cap}} + \frac{n_2}{\tau_{esc}} \tag{1}$$

$$\frac{dn_2}{d_t} = \frac{n_1}{\tau_{cap}} - \frac{n_2}{\tau_{esc}} - \frac{n_2}{\tau_n} - \frac{v_g G(n) S}{1 + \varepsilon_g S} \tag{2}$$

$$\frac{dS}{dt} = \left[\Gamma v_g \frac{G(n)}{1 + \varepsilon_g S} - \frac{1}{\tau_{ph}}\right] S \tag{3}$$

where $n_1$, $n_2$ are the carrier density in SCH and QW region, respectively; $S$ is the photon density; $\tau_n$ is the bimolecular recombination lifetime; $\tau_{ph}$ is the photon lifetime; $\tau_{cap}$ is the effective capture time considering both the transport of carriers across the SCH and QW region and captured by the QWs; $\tau_{esc}$ is the escape time, including thermal emission and diffusion time from the well to the SCH region; $\Gamma$ is the optical confinement factor, which is dependent on the interlayer thickness for hybrid lasers; $G(n)$ is the carrier density dependent gain; $v_g$ is the group velocity; $\varepsilon_g$ is the gain compression factor; $q_e$ is the electron unit charge; $V$ is the volume of SCH and active region; and $I$ is the injection current, respectively. For MQW devices, $\Gamma$ and $V$ are taken into consideration of the total confinement factor and volume of the active regions.

The small signal analysis of equations are solved by placing the following relations into the above rate equation model:

$$I = I_0 + \Delta I e^{i\omega t} \tag{4}$$

$$n_1 = n_{10} + \Delta n_1 e^{i\omega t} \tag{5}$$

$$n_2 = n_{20} + \Delta n_2 e^{i\omega t} \tag{6}$$

$$S = s_0 + \Delta S e^{i\omega t} \tag{7}$$

$$G = g_0 + g' \Delta n_2 e^{i\omega t} \tag{8}$$

where $g'$ is the differential gain, $n_{20}$ is the steady-state carrier density in the QW, and $g_0$ is a constant and is clamped at the steady state value of $n_{20}$. Substituting (4)–(8) into (1)–(3), the

steady state quantities can be obtained by setting the time-dependent terms to be zero. The resulting small-signal equations are as follows:

$$i\omega\Delta n_1 = \frac{\Delta I}{q_e V} - \frac{\Delta n_1}{\tau_{cap}} + \frac{\Delta n_2}{\tau_{esc}} \tag{9}$$

$$i\omega\Delta n_2 = \frac{\Delta n_1}{\tau_{cap}} - \frac{\Delta n_2}{\tau_{esc}} - \frac{\Delta n_2}{\tau_n} - v_g\frac{g_0\Delta S}{(1+\varepsilon_g s_0)^2} - v_g\frac{g'\Delta n_2 s_0}{1+\varepsilon_g s_0} \tag{10}$$

$$i\omega\Delta S = \frac{\Gamma v_g g' s_0 \Delta n_2}{1+\varepsilon_g s_0} - \frac{\varepsilon_g s_0}{(1+\varepsilon_g s_0)\tau_{ph}}\Delta S \tag{11}$$

where the Taylor expansion

$$\frac{1}{1+\varepsilon_g S} = \frac{1}{1+\varepsilon_g s_0} - \frac{\varepsilon_g s_0}{(1+\varepsilon_g s_0)^2}$$

and the steady-state solution of photon density equation

$$\frac{\Gamma v_g g_0}{1+\varepsilon_g s_0} = \frac{1}{\tau_{ph}}$$

are used. This set of small-signal equations can be obtained by eliminating $\Delta n_1$ and $\Delta n_2$ to give a relationship between the modulating current $\Delta I$ and optical output $\Delta S$:

$$\frac{\Delta S}{\Delta I} = \left(\frac{1}{1+i\omega\tau_{cap}}\right)\frac{\frac{\Gamma v_g g' s_0}{q_e V}}{\left\{i\omega\left[1+\left(\frac{\tau_{cap}}{1+i\omega\tau_{cap}}\right)\frac{1}{\tau_{esc}}\right]+\frac{v_g g' s_0}{1+\varepsilon_g s_0}+\frac{1}{\tau_n}\right\}\left[i\omega(1+\varepsilon_g s_0)+\frac{\varepsilon_g s_0}{\tau_{ph}}\right]+\frac{v_g g' s_0}{\tau_{ph}(1+\varepsilon_g s_0)}} \tag{12}$$

The modulation response is given by $M(w)$, where $M(\omega) = |\Delta S/\Delta I|$ can be written in a normalized form as follows:

$$\frac{M(\omega)}{M(0)} = \frac{\omega_r^2}{(1+i\omega\tau_{cap})\left(\omega_r^2-\omega^2+i\omega\gamma\right)} \tag{13}$$

$$\omega_r^2 = \frac{\left(\frac{v_g g'}{\chi}\right)s_0}{\tau_{ph}(1+\varepsilon_g s_0)}\left(1+\frac{\varepsilon_g}{v_g g'\tau_n}\right) \tag{14}$$

$$\gamma = \frac{\left(\frac{v_g g'}{\chi}\right)s_0}{(1+\varepsilon_g s_0)} + \frac{\varepsilon_g s_0}{\tau_{ph}(1+\varepsilon_g s_0)} + \frac{1}{\chi\tau_n} \tag{15}$$

Transport factor $\chi = 1 + (\tau_{cap}/\tau_{esc})$ has been introduced into the equations. In the modulation response, $w_r$ and $\gamma$ are usually referred to the relaxation frequency and damping rate, respectively, where the damping rate is controlled by the coefficient of the *iw*. Another factor is the *K* factor, which can be derived from the analytical expression above:

$$K = 4\pi^2\left(\tau_{ph} + \frac{\varepsilon_g}{\frac{v_g g'}{\chi}}\right) \tag{16}$$

## 3. Modulation Response

### 3.1. Temperature

For a typical SQW with a SCH layer as shown in Fig. 1, there are two mechanisms dominating the carrier transports from the doped cladding layers to the quantum well. The first one is the carrier transport across the SCH layer and captured by the quantum well [12]. The carrier transport across the SCH is governed by the classical current continuity equations, while the carriers captured by the quantum well is related to a quantum mechanical effect. This total lifetime is mainly determined by the carrier transport time due to the quick capture time, which has been shown to be in the subpicosecond time scale by time-resolved measurements in experiments [16], [17]. By solving the current continuity equations, the carrier transport lifetime can be written as

$$\tau_{cap} = \frac{1}{2}\left(\frac{d_{SCH}^2}{2D_p} + \frac{d_{SCH}^2}{2D_n}\right) \tag{17}$$

where is $d_{\mathrm{SCH}}$ the thickness of SCH region, and $D_p$ and $D_n$ are hole and electron diffusion coefficient, respectively. According to the Einstein relation:

$$D = \left(\frac{k_B T}{q_e}\right)\mu$$

where $k_B$ is Boltzmann constant, and $\mu$ is the mobility and which is material dependent. Due to the high electron mobility, the carrier transport time is mainly dominated by the hole diffusion time.

The second transport mechanism is the carrier escape from the quantum well to barrier bound state or continuum state in the cladding region. When devices are operated under high temperature, the thermal escape effect is significant and should be considered. According to the Boltzmann statistics, the thermionic emission lifetime $\tau_{esc}$ is an average of the electron and hole thermionic emission time according to the ambipolar carrier transport [12]. The thermionic emission time from a quantum well can be written as

$$\tau_{esc} = \left(\frac{2\pi m^* d_w^2}{k_B T}\right)\exp\left(\frac{E_B}{k_B T}\right) \tag{18}$$

where $E_B$ is the effective barrier height, and $m^*$ is the carrier mass. From this formula, we can see that thermionic emission is sensitive to barrier height and temperature. For the InGaAsP/InP materials, the barrier height is about 40% of the band offset between the quantum well and barriers, thus the carrier thermal escape effect is significant when the temperature is high. For the multi-quantum well structure considered here, another transport mechanism is the carrier tunneling between quantum wells. However, this tunneling mechanism is weak due to the relative thick barrier width. In this paper, in order to compare with experimental results, we consider the same structure and materials used in [10] unless it is specified. The structure and material parameters of hybrid lasers used in the calculation are listed in the Tables 1 and 2, respectively. Some parameters come from [18].

In hybrid lasers, the III–V materials are bonded to the patterned SOI water by wafer bonding technique. During the wafer bonding, the thickness of the bonding interlayer should be carefully designed. A thin or free bonding interlayer ($SiO_2$ or BCB photoresist) between III–V materials and SOI waveguide is beneficial to the light coupling into the Si waveguide from III–V waveguide. However, thick interlayer is usually preferred for good bonding quality. Thus, there is a tradeoff between the light coupling efficiency and the bonding quality. In addition, the commercial SOI chip usually has a thick $SiO_2$ BOX layer (1–2 $\mu$m) with a high thermal resistance. Thus, effective heating dissipation is difficult to be achieved in hybrid lasers due to the poor thermal conductivity of $SiO_2$ beneath and above the Si waveguide. To investigate the strong heat effect

TABLE 1

The structure of the test laser [10]

| | | |
|---|---|---|
| III-V Well | Number of wells 6<br>Materials InGaAsP<br>Width 8 nm | SCH width 80 nm<br>III-V stripe width 1.7μm<br>Cavity length 500 μm |
| III-V Barrier | Materials InGaAsP<br>Number of barriers 5 | Width 10 nm |
| Si | Si width 1 μm<br>Interlayer thickness 0 μm | Si Height 340 nm |

TABLE 2

Parameters for the InGaAsP/InP used in calculations [18]

| Parameter | symbol | Unit | value |
|---|---|---|---|
| Mirror reflectivity | R | - | 0.32 |
| Gain compression factor | $\varepsilon_g$ | $cm^{-1}$ | $1.5\times10^{-17}$ |
| Differential gain | $g'$ | $cm^{-1}$ | $3\times10^{-16}$ |
| Intrinsic loss | $\alpha_i$ | $cm^{-1}$ | 15 |
| Group velocity | $v_g$ | cm/s | $8.5\times10^{9}$ |
| Electron mobility | $\mu_n$ | $cm^2$/vs | 3000 |
| Hole mobility | $\mu_p$ | $cm^2$/vs | 180 |
| Bimolecular recombination lifetime | $\tau_n$ | ps | 0.1 |
| Effective barrier height | $E_B$ | eV | 0.104 |

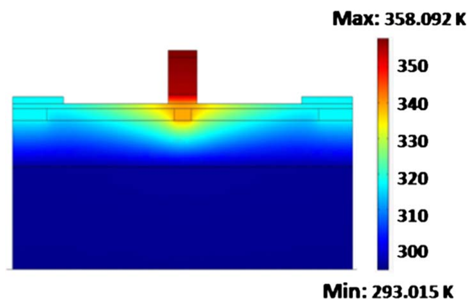


Fig. 2. Thermal profile for the waveguide cross sections under 200 mA of injection current.

of hybrid lasers, all of the carrier diffusion /capture, thermionic escapes lifetimes are temperature dependent in the simulations.

A 2-D model of the hybrid lasers structure was conducted to investigate the thermal characteristics of the hybrid structures without any interlayer between III/V and Si interface, as shown in Fig. 2. The SOI structure consists of a Si substrate, a 2 $\mu$m-thick $SiO_2$ lower cladding layer,

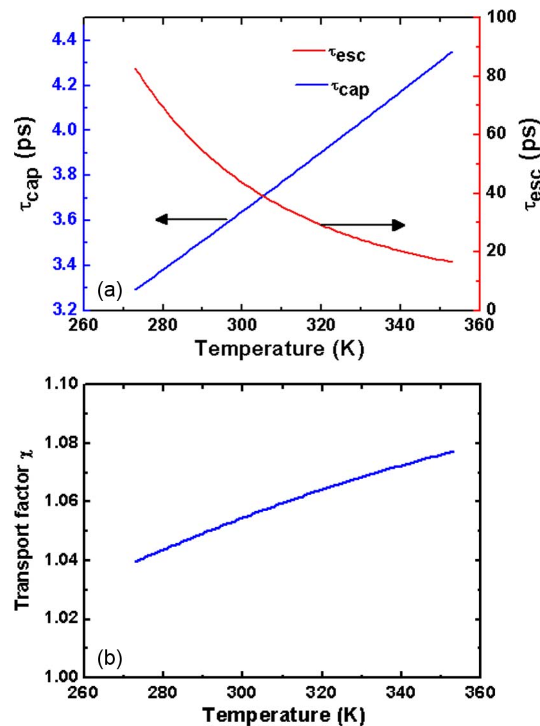


Fig. 3. Carrier escape, capture lifetime (a) as well as transport factor (b) vs. the temperature.

and a Si ridge waveguide with a height (H), width (W) of 0.34 $\mu$m and 1 $\mu$m, respectively. The III–V mesa width is fixed at 1.7 $\mu$m, as listed in Table 1. Heat is generated by Joule heating. The maximum of temperature in the active region can reach to 358 K under an injection current of 200 mA. If there is an interlayer between the interfaces, the temperature will be higher. From Fig. 2, most of the heat is kept in the III–V region, and the heat can only be dissipated by the narrow Si waveguide channel due to the low thermal conductivity of the buried oxide lower cladding. Since transverse heat flow directly down the device is limited by the oxide thickness, lateral heat flow becomes an important mode of heat extraction. Thermal shunt circuit have been proposed on the sides of the device by etching though the silicon waveguide layer and the lower dioxide cladding layer and filling the void with materials with higher thermal conductivity [19]. Thus the temperature plays a vital role for hybrid lasers under high speed modulations. In fact, when laser operates, the temperature rising in the active region becomes even more severe due to the nonradiative recombination and carrier leakage. This will further degrade the differential gain and reduce the modulation speed. Therefore, improving the laser design to decrease the threshold current and increase the heat dissipation is expected to significantly improve the modulation bandwidth of hybrid lasers.

The temperature dependence of the carrier capture and escape lifetime is shown in Fig. 3(a). The carrier capture lifetime rises linearly and the escape lifetime exponentially decreases with the temperature. This is easily understood according to (17) and (18). The capture and escape times are in few and tens picoseconds ranges, respectively, which are close to the measured data [20]. This absolute times difference between both causes the transport factor slightly varied with the increasing temperature, as shown in Fig. 3(b), but it can affect the modulation response significantly, which has been proved in [21]. According to (14) and (15), this will decrease the relaxation frequency and damping rate simultaneously.

The frequency response at different temperatures is calculated. In the simulation, the injection current and SCH thickness are of 100 mA and 80 nm, respectively. As shown in Fig. 4, the bandwidth decreases from 6.2 GHz to 2.2 GHz when the temperature increases from 300 K to

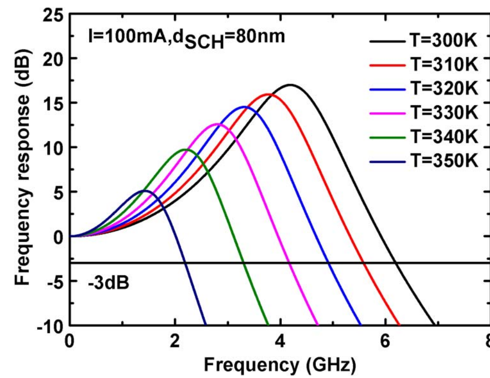


Fig. 4. Modulation bandwidth of hybrid lasers under different temperatures with an injection current of 100mA and 80nm SCH layer.

350 K in a step of 10 K. This is due to the larger transport factor caused by the faster carrier escape rate with a higher temperature. Furthermore, in Fig. 4, we can see that the peak of relaxation frequency is lower at high temperatures, and this is coincident with practical measurement. It is worth to be mentioned that the ultimate modulation bandwidth is determined by both the relaxation resonance frequency and the damping rate. The bandwidth will increase if the $w_r$ is large with strong damping rate $\gamma$, and a relative flat response can be achieved [22], [23].

### 3.2. Confinement Factor

The bonded structure forms a hybrid waveguide, whose optical mode lie in both the III–V structure and the silicon waveguide. The coupling between the two waveguides plays an important role. In literature, there are two solutions reported. In the first approach, based on the evanescent coupling, most part of the optical field locates in the silicon waveguide and only a few percent of the optical mode, overlaps with the III–V MQW region [7], [8]. A high confinement in III–V materials will be beneficial to a low threshold current, but this leads to a low output coupling efficiency. Hence, there is a trade-off on the laser performance due to the optical confinement factor for this overlapped structure. The confinement factors in III–V and silicon regions of the hybrid waveguide can be controlled by changing the silicon waveguide width and height. However, it requires a thin bonding layer ($\sim$10 nm) in order for efficient optical coupling, which may increase the difficulty of bonding process. The waveguide structure is shown in Table 1. Even for the second approach, where the optical mode is mostly confined in the III–V material realized by adiabatically tapering the silicon and III–V waveguides, there is a critical interlayer thickness in order to achieve a high coupling efficiency [9]. As mentioned in the introduction section, the confinement factor of hybrid lasers is related to the thickness of interlayer between III–V materials and SOI, the effect of interlayer thickness will be demonstrated by the confinement factor in the rate equations. The confinement factor is calculated by the two dimensional finite-difference method. Fig. 5(a) shows the confinement factor versus interlayer thickness for the different Si thickness in SOI. The confinement factor increases when the Si depth changes from 340 nm to 500 nm, because more light will be confined in the III–V waveguide. Similarly, the modulation response shows the same trend versus the interlayer thickness, as shown in the Fig. 5(b). Therefore, a thinner interlayer can increase both the light coupling efficiency and the response bandwidth.

### 3.3. SCH Thickness

In the carrier transport model as described in the first section, the SCH thickness has a significant effect on the carrier capture time. For example, the $-3$ dB bandwidth of the modulation response decreases significantly from 8.6 GHz to 4.7 GHz when the SCH thickness increases from 20 nm to 140 nm as a step of 20 nm, as shown in Fig. 6. This is because the carriers

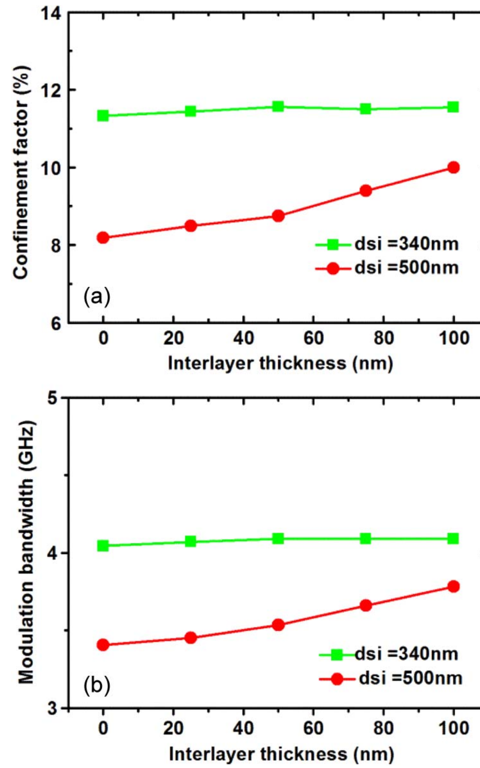


Fig. 5. Confinement factor (a) and modulation bandwidth (b) vs. interlayer thickness of the different Si depth.

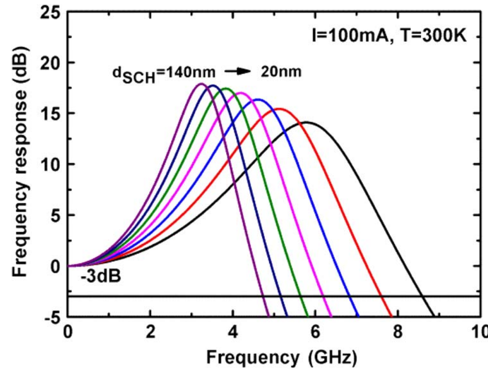


Fig. 6. Modulation bandwidth under the different thicknesses of SCH layer at room temperature.

capture rate increases with the decreasing SCH thickness, which is easy to be understood according to (17). Simultaneously, both the resonance frequency and damping rate decrease with the increasing SCH layer thickness, which is due to the smaller transport factor, as shown by the red line in Fig. 7.

Generally, the K factor determines the maximum possible modulation bandwidth according to the formula

$$f_{\max} = \frac{2\pi\sqrt{2}}{K} \tag{19}$$

As shown by the blue line in Fig. 7, $f_{\max}$ decreases significantly with the increasing SCH thickness, while totally reverse trend is found for the transport factor variation with the SCH

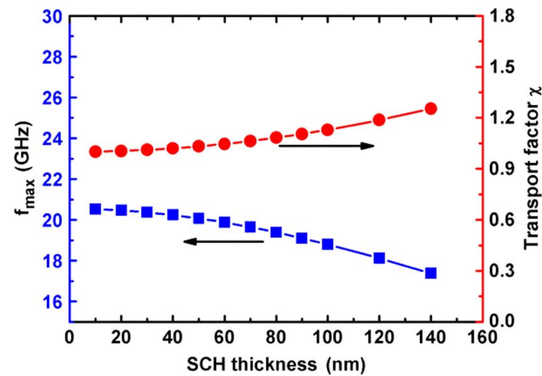


Fig. 7. Maximum modulation bandwidth and transport factor vs. SCH thickness.

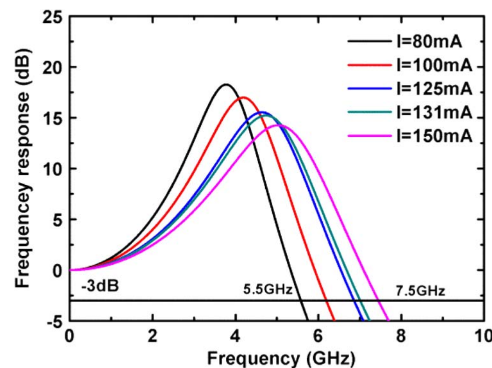


Fig. 8. Frequency response under the different bias current at room temperature.

thickness. This is attributed to the increasing carrier capture and the diffusion times for the thicker SCH layer, leading to smaller −3 dB bandwidth. Compared with the simulation results in Figs. 6 and 7, we can see the ideal maximum modulation bandwidth is much larger than the practical one considering carrier transport effects. More importantly, SCH layer thickness plays a dominate role on the bandwidth compared with other factors. For the hybrid lasers, thin P type SCH can increase the modulation bandwidth and the coupling efficiency between the III–V and SOI. Recently, this technique has been utilized in short cavity DFB lasers by UCSB, and the modulation speed is increased significantly [24].

In addition, to verify our model and simulation, the dependence of the frequency response on the injection current is also studied and compared with the experimental modulation bandwidth in [10]. Fig. 8 shows the frequency response under the different bias current at room temperature. As shown in Fig. 8, with the bias current increasing, the modulation bandwidth increases. The −3 dB bandwidth increases with injection rising and reaches to 7.1 GHz under the injection current of 131 mA at room temperature, which matches well with experimental data (about 7.2 GHz) in [10].

### 3.4. Eye Diagram

The large-signal dynamic response of a semiconductor lasers is very complicated due to the high nonlinear properties of the devices. Eye diagram is an effective way to characterize the quality of the large signal response by observing the degree of eye opening, which is an indicator of the modulation performance. The large signal response can be related directly to the small-signal bandwidth, which has been theoretically predicated and verified by experiments [25].

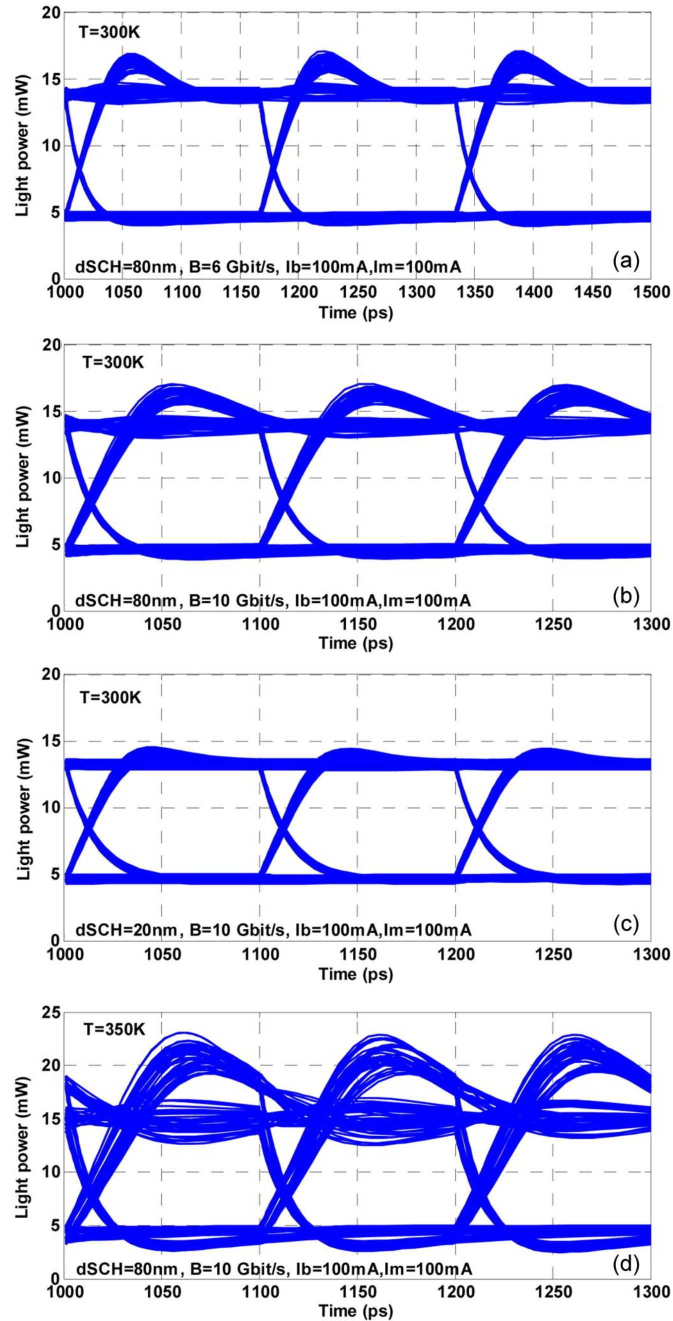


Fig. 9. Illustrative figure of a 3-bit-long eye diagram for (a) $d_{SCH} = 80$ nm, B = 6 Gbit/s; (b) $d_{SCH} = 80$ nm, B = 10 Gbit/s; (c) $d_{SCH} = 20$ nm, B = 10 Gbit/s; and (d) $d_{SCH} = 80$ nm, B = 10 Gbit/s as $I_b = 100$ mA, and $I_m = 100$ mA. (a)–(c) are simulated at T = 300 K, and (d) is simulated at T = 350 K.

A theoretical simulation of the eye diagram of hybrid lasers subjected to pseudorandom digital modulation at gigabit rates is presented based on the rate equation model [25]. The injection current $I$ comprises two parts:

$$I = I_b + I_m f_m(t) \tag{20}$$

where the first part is the direct bias current, the second part represents modulation current which decides the modulation depth of the laser, and $f_m(t)$ is a time varying function with digital

0 or 1 describing the bit format of the modulating current. Usually, the bit format is based on either NRZ or RZ pseudorandom bit generation. In the simulations, the rate equations are solved numerically by means of the fourth-order Runge–Kutta method assuming square pulses of the modulating current in equation (18). The eye diagram is constructed by dividing the output light power into 3-bit long sequences and overlying each other.

Fig. 9 shows the eye diagram simulated with different conditions under the same biasing current $I_b = 100$ mA and $I_m = 100$ mA, when the threshold current of the hybrid laser is the same 60 mA as that in small signal analysis. As shown in Fig. 9(a) and (b), the relaxation oscillation occurs under both 6 and 10 Gbit/s modulation rate. When the modulation rate is 6 Gbit/s, the light response can keep pace with the electrical signal variation, so the eye diagram is open clearly. This is consistent with the frequency response in the small signal analysis and the experimental values in [26]. However, when the modulation frequency increases to 10 Gbit/s, the delay of optical responses appears, although the eye diagram is open clearly with a thicker eyelid. If the modulation rate is further increased to 16 Gbit/s, the eye diagram will be entirely closed.

To further investigate the effect of SCH thickness on the large-signal response, the eye diagrams with $d_{SCH} = 20$ and 80 nm are simulated at $T = 300$ K under a modulation rate of 10 Gbit/s, as shown in Fig. 9(b) and (c). Compared with Fig. 9(b) and (c), it can be seen that the relaxation oscillation in the 1 level is suppressed with thinner SCH thickness, and the eye diagram is open. It is attributed to the low turn-on jitter from the faster carrier capture rate with a thinner SCH thickness. This trend is consistent with the results of small signal frequency analysis.

Temperature plays a dominate role in small-signal response, as discussed in section A. Here, we also studied the dependence of the quality of eye diagram on the temperature in large signal response. Fig. 9(d) shows the eye diagram simulated under $T = 350$ K while keeping $B = 10$ Gbit/s, $d_{SCH} = 80$ nm. The strong overshot is found and the eye diagram is partially closed, in contrast with Fig. 9(b). In addition, the timing jitter appears due to the increasing optical response delay while the extinction ratio decreases from 4.2 dB to 3.7 dB as the temperature rising from 300 K to 350 K. It is well known that the eye diagram is a simple visual tool to examine the quality of the modulated signal. Combined with the results in Fig. 4, the effect of temperature on the high speed modulation is emphasized clearly.

## 4. Conclusion

The dynamic responses of hybrid lasers are studied with the carrier transport model. The simulation results are coincident with published experimental data based on this simple model. It is found out that the limitations on the direct modulation speed of long wavelength hybrid lasers are mainly caused by the carrier transport time, temperature, confinement factor, and SCH thickness. The frequency response of the small signal analysis shows that the modulation bandwidth is particularly sensitive to the operation temperature, as well as the SCH thickness. More specifically, the highest modulation bandwidth decreases from 6.2 GHz to 2.2 GHz under an injection current of 100 mA and an 80 nm SCH layer when the temperature increases from 300 K to 350 K. However, the modulation bandwidth can be improved up to about 4 GHz with increasing 120 nm-thick SCH layer. For hybrid lasers, to increase the modulation bandwidth, a thin P-type SCH layer can be beneficial. In addition, the effects of confinement factor on the frequency response are also studied under different interlayer thickness for 340 nm and 500 nm Si depths. Finally, eye diagrams are calculated under different bit rates, SCH thicknesses and temperatures, respectively. The overshot is suppressed by decreasing the SCH thickness and the eye diagram become partially close with temperature increasing. The optimized modulation speed can reach to 10 Gbit/s at $T = 300$ K.

## Acknowledgement

The authors would like to thank Dr. H. Ji for help with the program used to calculate the eye diagram.

## References

[1] R. Nagarajan and M. Smit, “Photonic integration,” *IEEE LEOS Newslett.*, vol. 21, no. 3, pp. 4–10, Jun. 2007.
[2] R. Nagarajan *et al.*, “Large-scale photonic integrated circuits,” *IEEE J. Sel. Top. Quantum Electron.*, vol. 11, no. 1, pp. 50–65, Jan./Feb. 2005.
[3] R. Nagarajan *et al.*, “Single-chip 40-channel InP transmitter photonic integrated circuit capable of aggregate data rate of 1.6 Tbit/s,” *Electron. Lett.*, vol. 42, no. 13, pp. 771–773, Jun. 2006.
[4] M. Kato *et al.*, “40-channel transmitter and receiver photonic integrated circuits operating at per channel data rate 12.5 Gbit/s,” *Electron. Lett.*, vol. 43, no. 8, pp. 468–469, Apr. 2007.
[5] R. Nagarajan *et al.*, “Monolithic, 10 and 40 channel InP receiver photonic integrated circuits with on-chip amplification,” presented at the Opt. Fiber Commun. Conf., Anaheim, CA, USA, Mar. 2007, Paper PDP32.
[6] A. W. Fang *et al.*, “Electrically pumped hybrid AlGaInAs–silicon evanescent laser,” *Opt. Exp.*, vol. 14, no. 20, pp. 9203–9210, Oct. 2006.
[7] A. W. Fang *et al.*, “Integrated AlGaInAs silicon evanescent race track laser and photodetector,” *Opt. Exp.*, vol. 15, no. 5, pp. 2315–2322, Mar. 2007.
[8] A. W. Fang *et al.*, “A distributed feedback silicon evanescent laser,” *Opt. Exp.*, vol. 16, no. 7, pp. 4413–4419, Mar. 2008.
[9] S. Keyvaninia *et al.*, “Demonstration of a heterogeneously integrated III–V/SOI single wavelength tunable laser,” *Opt. Express*, vol. 21, no. 3, pp. 3784–3792, Feb. 2013.
[10] G. H. Duan *et al.* “Hybrid III–V on silicon lasers for photonic integrated circuits on silicon,” *IEEE J. Sel. Topics Quantum Electron.*, vol. 20, no. 4, Jul./Aug. 2014, Art. ID. 6100213.
[11] W. Rideout *et al.*, “Well-barrier hole burning in quantum well lasers,” *IEEE J. Quantum Electron.*, vol. 3, no. 9, pp. 784–786, Sep. 1991.
[12] R. Nagarajan, T. Fukushima, R. S. Geels, and J. E. Bower, “High speed quantum-well lasers and carrier transport effects,” *IEEE J. Quantum Electron.*, vol. 28, no. 10, pp. 1990–2008, Oct. 1992.
[13] T. Keating, X. Jin, S. L. Chuang, and K. Hess, “Temperature dependence of electrical and optical modulation responses of quantum well lasers,” *IEEE J. Quantum Electron.*, vol. 35, no. 10, pp. 1526–1534, Oct. 1999.
[14] G.-R. Lin *et al.*, “Long-cavity Fabry–Pérot laser amplifier transmitter with enhanced injection-locking bandwidth for WDM-PON application,” *J. Lightw. Technol.*, vol. 28, no. 20, pp. 2925–2932, Oct. 2010.
[15] S. Tarucha and K. Otsuka, “Response of semiconductor laser to deep sinusoidal injection current modulation,” *IEEE J. Quantum Electron.*, vol. 17, no. 5, pp. 810–816, May 1981.
[16] G. Eisenstein *et al.*, “Ultrafast gain dynamics in 1.5 $\mu$m multiple quantum well optical amplifiers,” *App Phys. Lett.*, vol, 58, no. 2, pp. 158–160, Jan. 1991.
[17] S. Weiss *et al.*, “Carrier capture times in 1.5 $\mu$m-multiple quantum well optical amplifiers,” *Appl. Phys. Lett.*, vol, 60, no. 1, pp. 9–11, Jan. 1992.
[18] M. C. Tatham, I. F. Lealman, C. P. Seltzer, L. D. Westbrook, and D. M. Cooper, “Resonance frequency, damping, and differential gain in 1.5 $\mu$m multiple quantum-Well lasers,” *IEEE J. Quantum Electron.*, vol, 28, no. 2, pp. 408–414, Feb. 1992.
[19] G. Roelkens *et al.*, “III–V/silicon photonics for on-chip and intra-chip optical interconnects,” *Laser Photon. Rev.*, vol. 4, no. 6, pp. 751–779, Nov. 2010.
[20] G. Eisenstein *et al.*, “Ultrafast gain dynamics in 1.5 m multiple quantum well optical amplifiers,” *Appl. Phys. Lett.*, vol, 58, no. 2, pp. 158–160, Jan. 1991.
[21] M. Ishikawa, R. Nagarajan, T. Fukushima, J. G. Wasserbauer, and J. E. Bowers, “Long wavelength high-speed semiconductor lasers with carrier transport effects,” *IEEE J. Quantum Electron.*, vol. 28, no. 10, pp. 2230–2241, Oct. 1992.
[22] R. S. Tucker, “High-speed modulation of semiconductor lasers,” *J. Lightw. Technol.*, vol. 3, no. 6, pp. 1180–1192, Dec. 1985.
[23] M. P. van Exter, W. A. Hamel, J. P. Woerdman, and B. R. P. Zeijlmans, “Spectral signature of relaxation oscillations in semiconductor lasers,” *IEEE J. Quantum Electron.*, vol. 28, no. 6, pp. 470–1478, Jun. 1992.
[24] C. Zhang *et al.*, “Low threshold and high speed short cavity distributed feedback hybrid silicon lasers,” *Opt. Exp.*, vol. 22, no. 9, pp. 10202–10209, May 2014.
[25] M. Ahmed, M. Yamada, and S. W. Mahmoud, “Analysis of semiconductor laser dynamics under gigabit rate modulation,” *J. Appl. Phys.*, vol. 101, no. 3, Feb. 2007, Art. ID. 033119.
[26] J.-M. Fedeli *et al.*, “InP on SOI devices for optical communication and optical network on chip,” *SPIE*, vol. 7942, Jan. 2013, Art. ID. 794200.